Supporting Information

Rapid Proton Transport through a Bio-inspired PO_4-Built Protective Layer for Stabilizing 5-Hydroxymethylfurfural Conversion at High Current Densities

Wei Ji [a], Wenjie Zhang [a], Chen Deng [b,c*], Yuwei Xiong [b], Qi Hao [d], Hao Zhang [e], Bing Song [f], Wenlei Zhu [g], Dekui Shen [a], Jason Chun-Ho Lam [h*], Richen Lin [a*]

[a] *Key Laboratory of Energy Thermal Conversion and Control of Ministry of Education, School of Energy and Environment, Southeast University, Nanjing 211189, China*

[b] *School of Chemistry and Chemical Engineering, Southeast University, Nanjing 211189, China*

[c] *Department of Electrical Engineering and Electronics, University of Liverpool, Liverpool L69 3GJ, UK*

[d] *Key Laboratory of Quantum Materials and Devices of Ministry of Education, School of Physics, Southeast University, Nanjing 211189, China*

[e] *State Key Laboratory of Clean Energy Utilization, Zhejiang University, Hangzhou 310027, China*

[f] *Scion, Te Papa Tipu Innovation Park, 49 Sala Street, Private Bag 3020, Rotorua 3046, New Zealand*

[g] *State Key Laboratory of Water Pollution Control and Green Resource Recycling, School of the Environment, Nanjing University, Nanjing 210023, China*

[h] *School of Energy and Environment, City University of Hong Kong, Kowloon Tong, Hong Kong SAR, 999077, China*

*Correspondence e-mail: richenlin@seu.edu.cn (R. Lin); jason.lam@cityu.edu.hk (J. Lam)

Supporting Figures and Tables

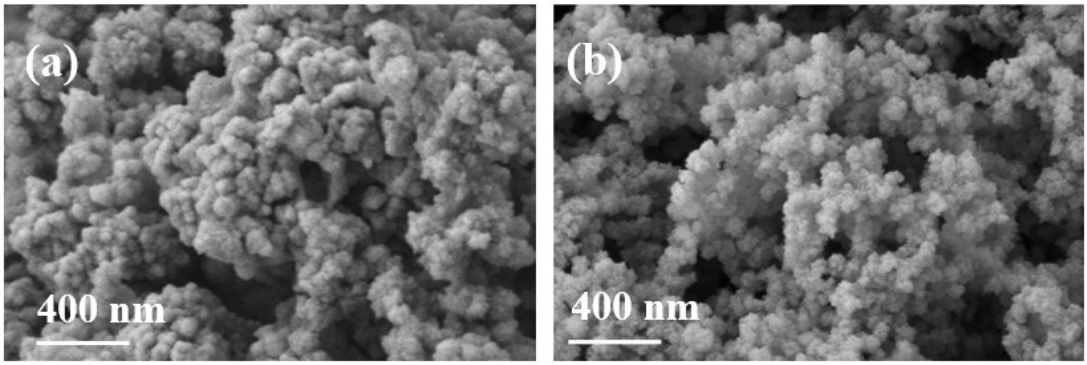

Figure S1. The SEM result of (a) CuNiO and (b) PO_4-BPL/CuNiO

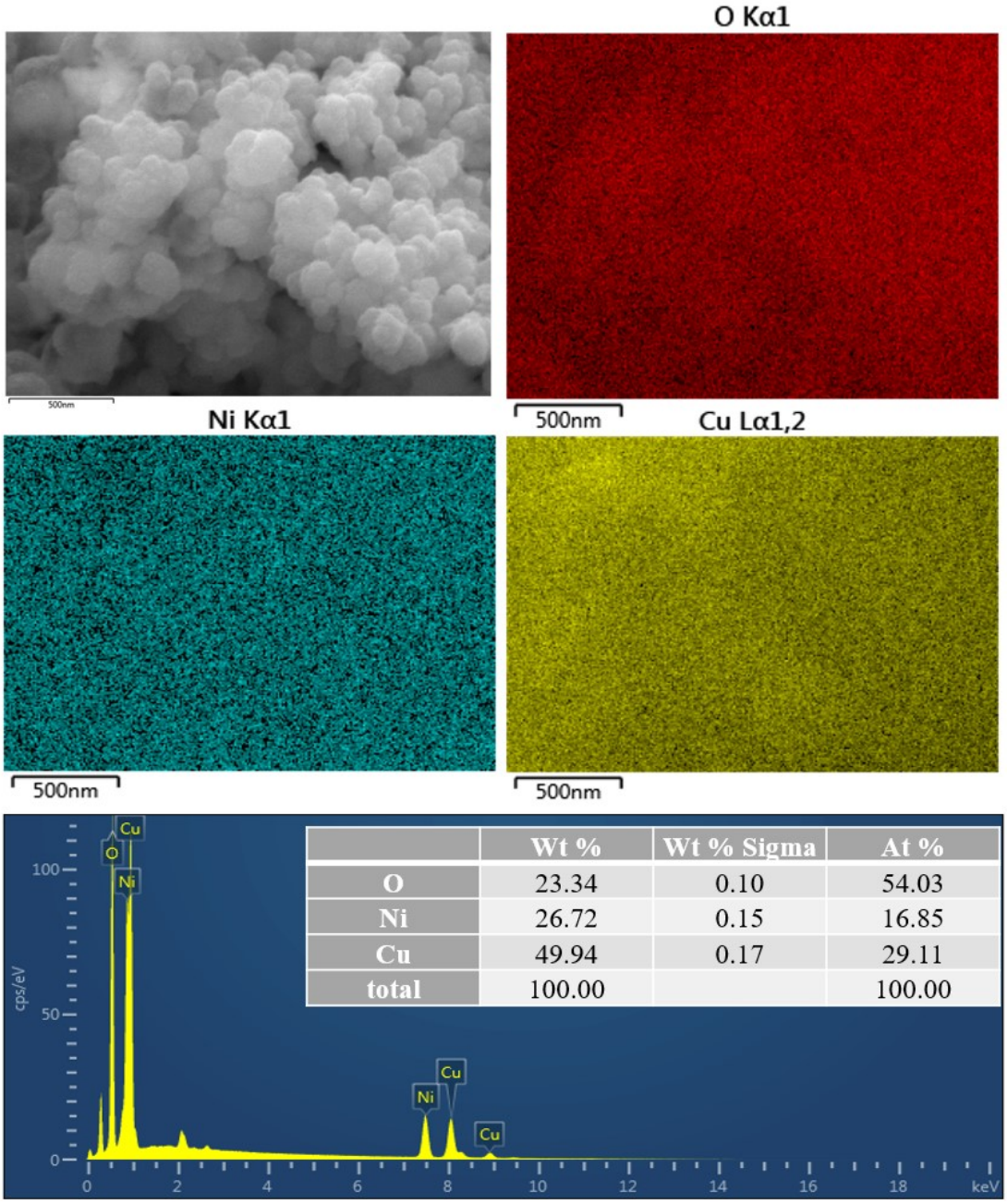

	Wt %	Wt % Sigma	At %
O	23.34	0.10	54.03
Ni	26.72	0.15	16.85
Cu	49.94	0.17	29.11
total	100.00		100.00

Figure S2. The SEM-EDS result of CuNiO

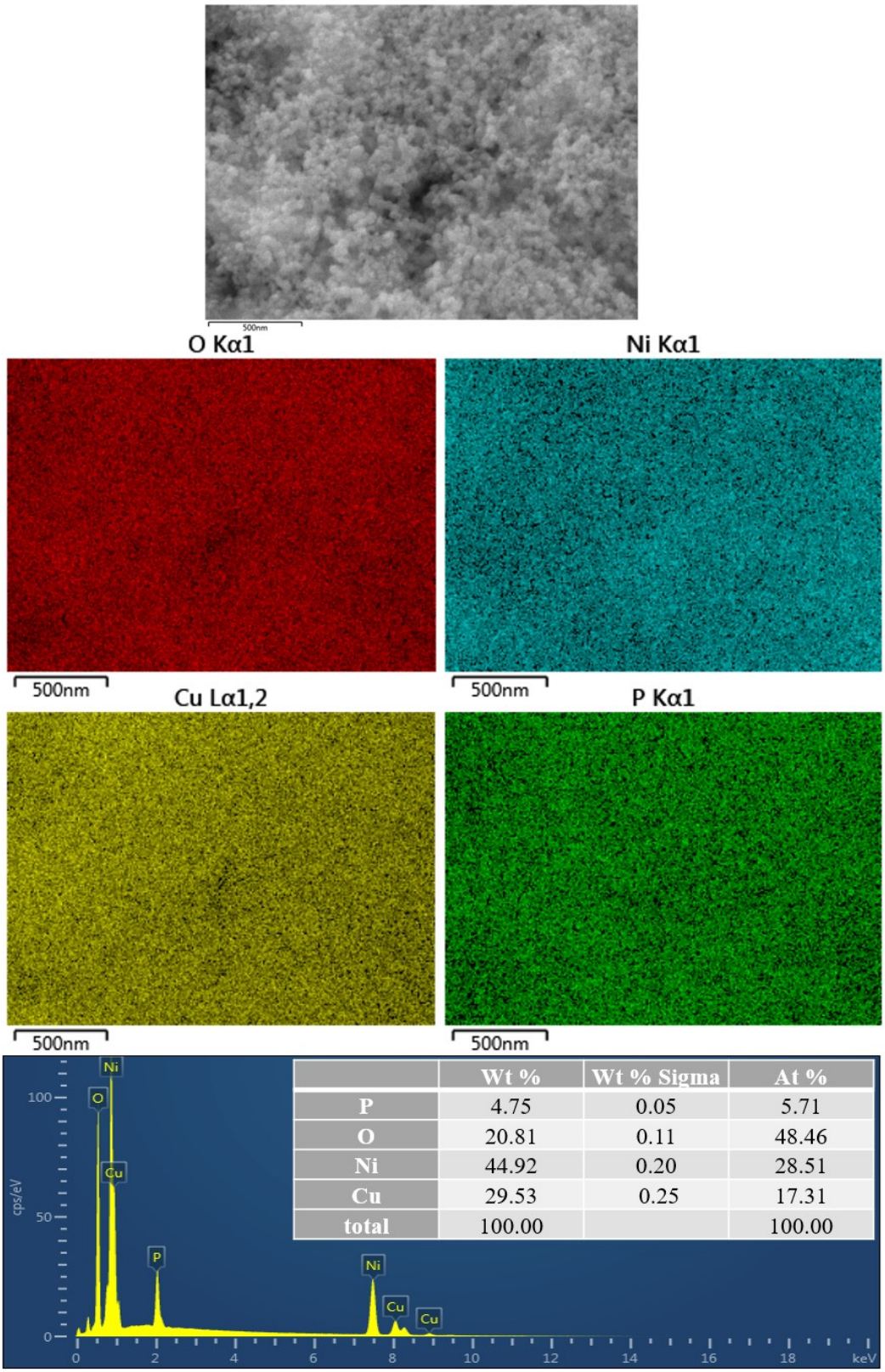

	Wt %	Wt % Sigma	At %
P	4.75	0.05	5.71
O	20.81	0.11	48.46
Ni	44.92	0.20	28.51
Cu	29.53	0.25	17.31
total	100.00		100.00

Figure S3. The SEM-EDS result of PO_4-BPL/CuNiO

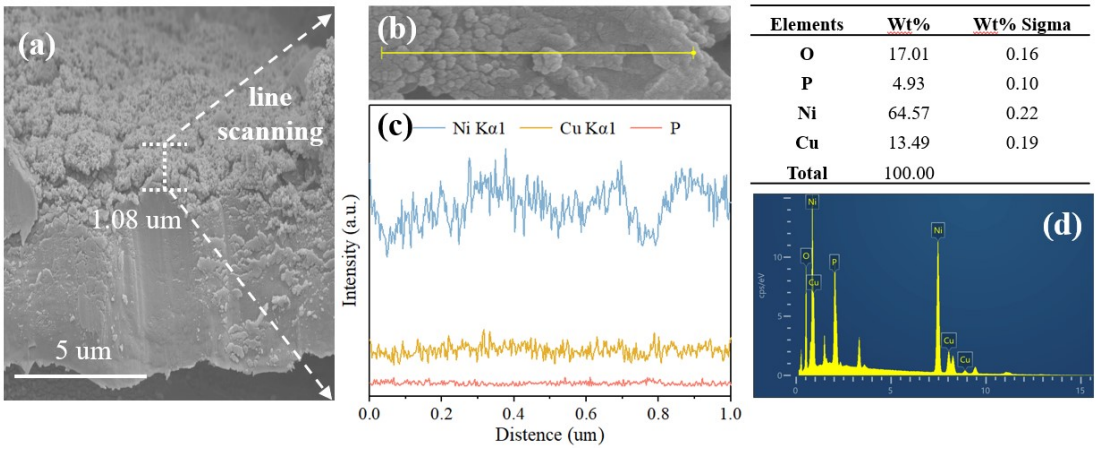

Elements	Wt%	Wt% Sigma
O	17.01	0.16
P	4.93	0.10
Ni	64.57	0.22
Cu	13.49	0.19
Total	100.00	

Figure S4. Results of SEM-EDS cross-sectional imaging.

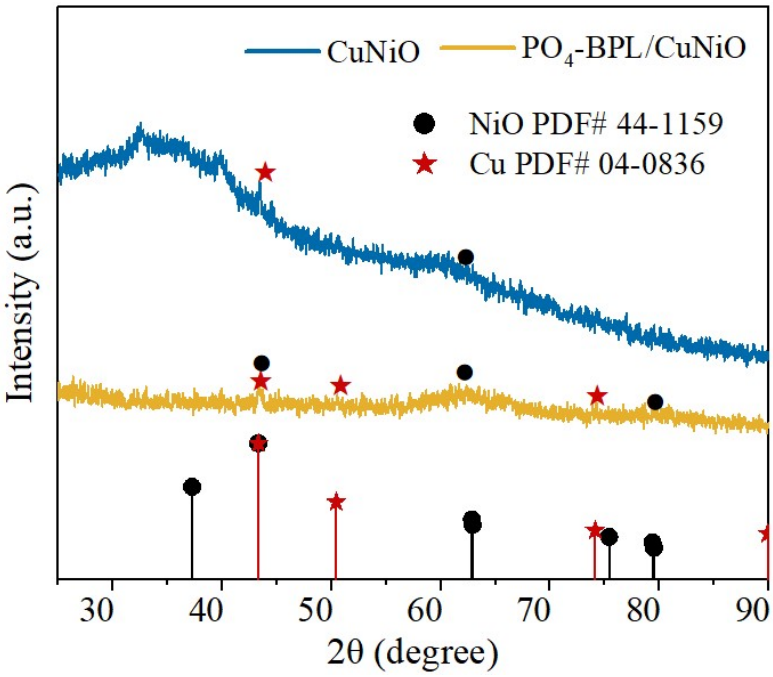

Figure S5. XRD results of PO_4-BPL/CuNiO and CuNiO

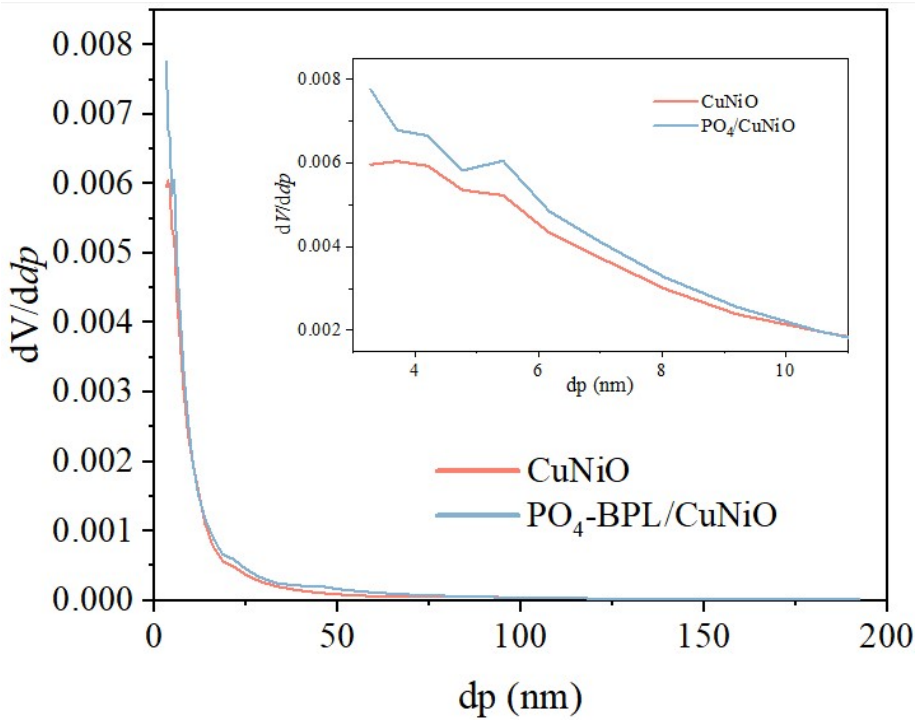

Figure S6. Results of pore size distribution

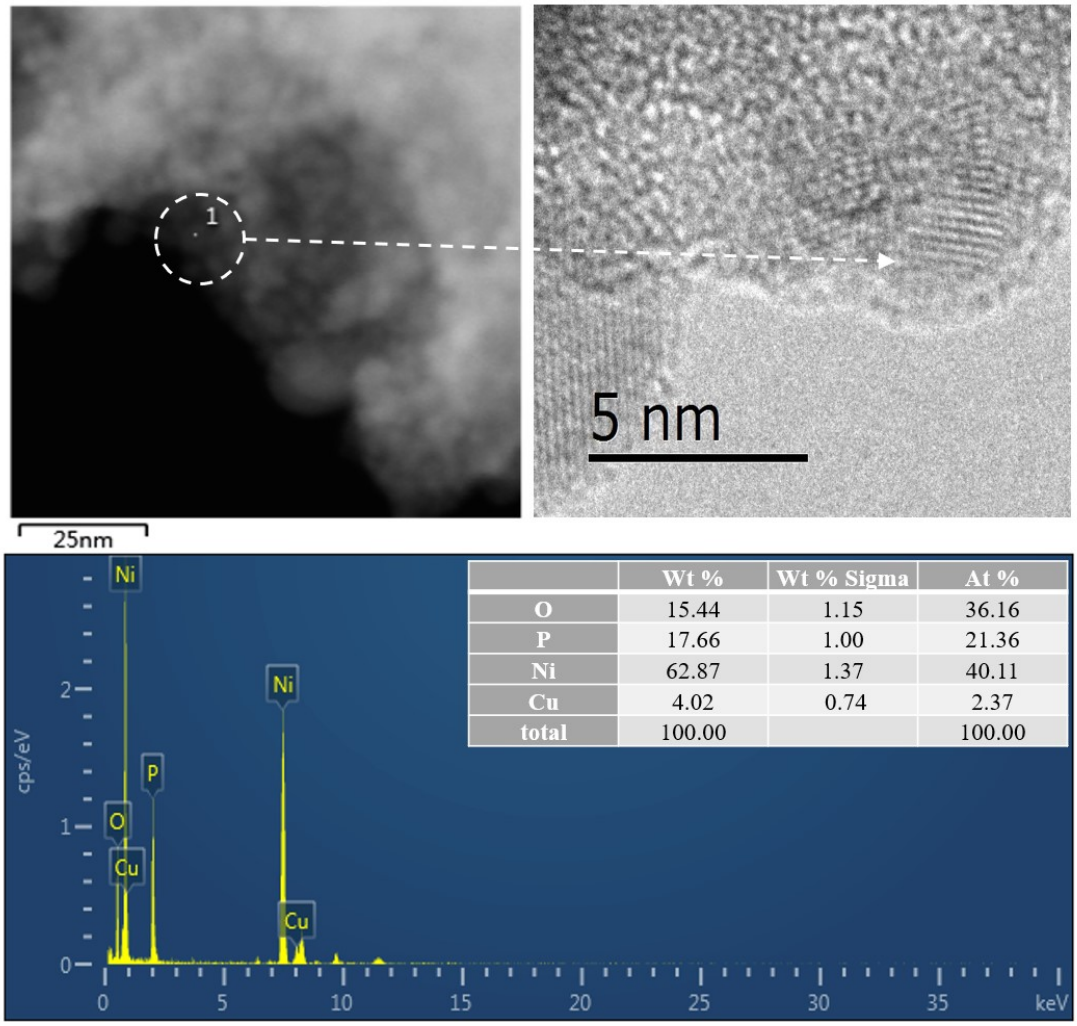

	Wt %	Wt % Sigma	At %
O	15.44	1.15	36.16
P	17.66	1.00	21.36
Ni	62.87	1.37	40.11
Cu	4.02	0.74	2.37
total	100.00		100.00

Figure S7. Results of point scanning at the lattice fringe

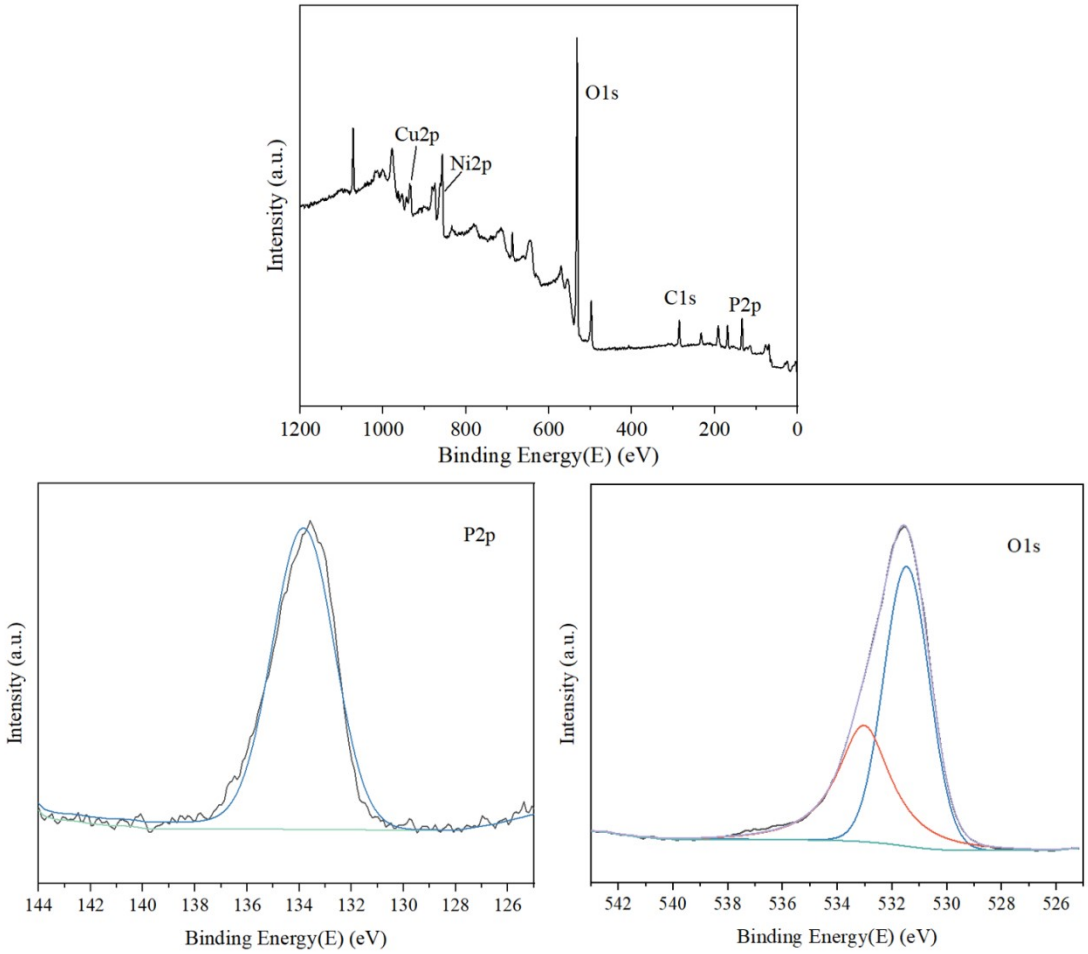

Figure S8. XPS results of PO_4-BPL/CuNiO

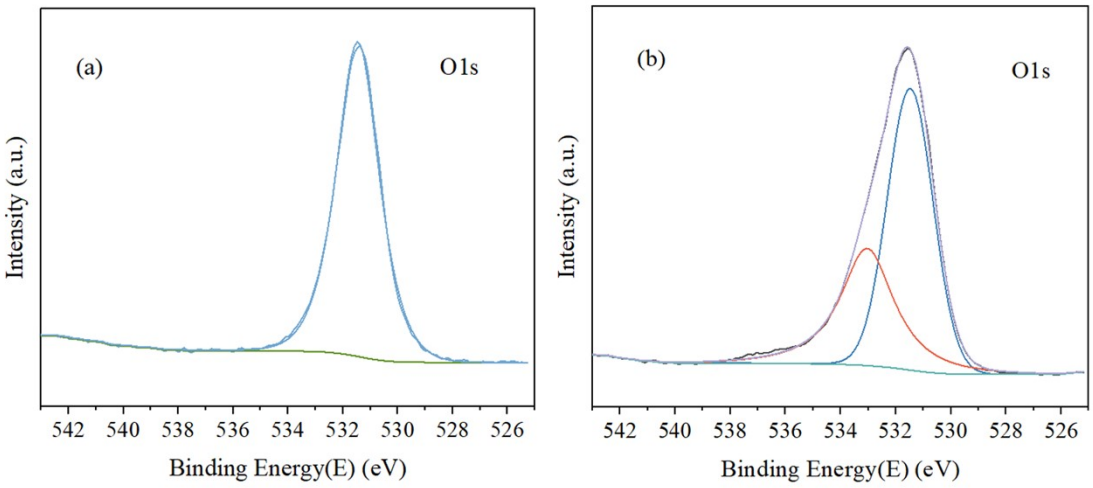

Figure S9. O 1s XPS results of (a) CuNiO and (b) PO_4-BPL/CuNiO

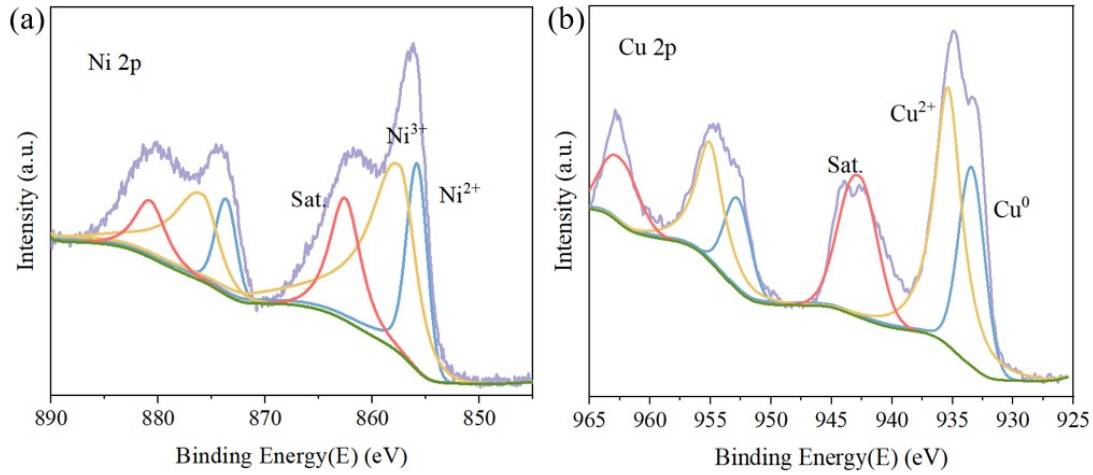

Figure S10 XPS peak fitting results of Cu and Ni elements in CuNiO: (a) Ni 2p; (b) Cu 2p.

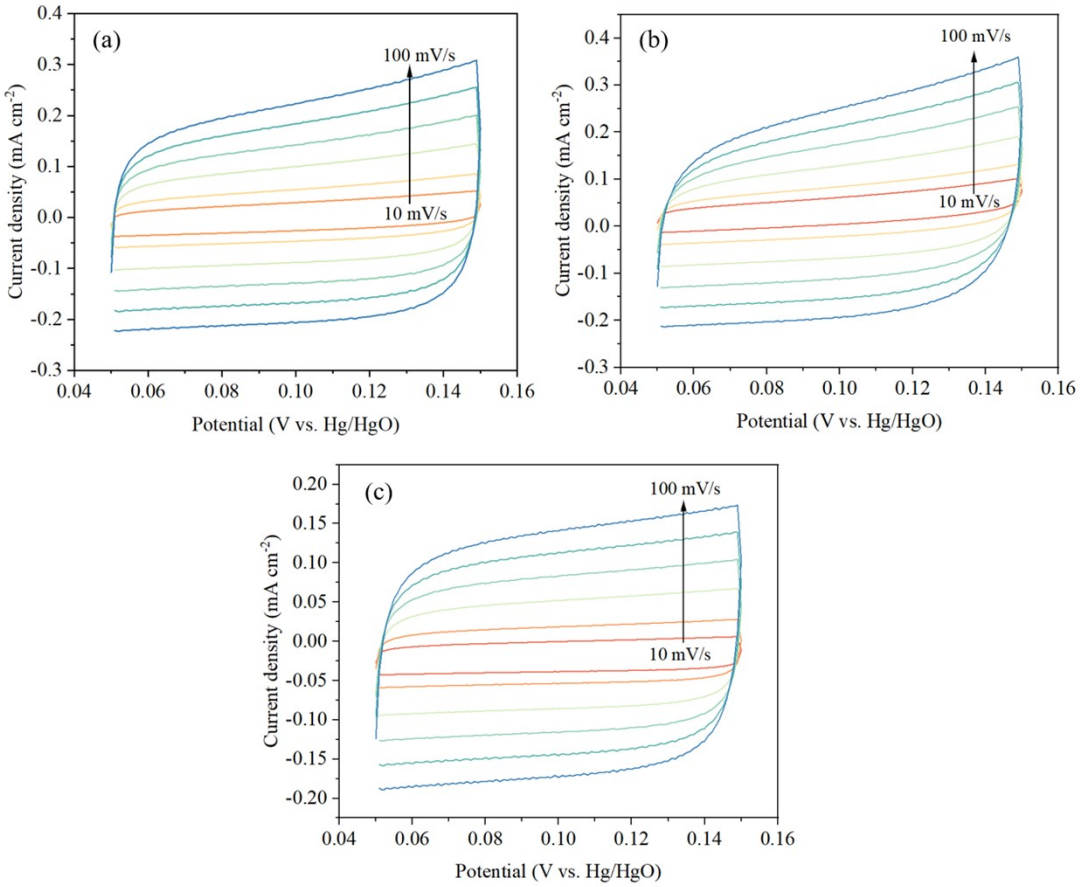

Figure S11. Determination of ECSA. CV curves of (a) CuNiO, (b) PO_4-BPL/NiO, (c) PO_4-BPL/CuNiO.

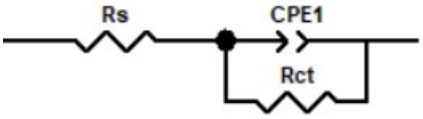

Figure S12. Equivalent fitting circuit diagram

Table S1. Values of equivalent fitting circuit diagram

	CuNiO	PO_4-BPL/CuNiO
Rs	1.39	1.44
CPE1-T	0.116	0.121
CPE1-P	0.782	0.769
Rct	2.43	1.67

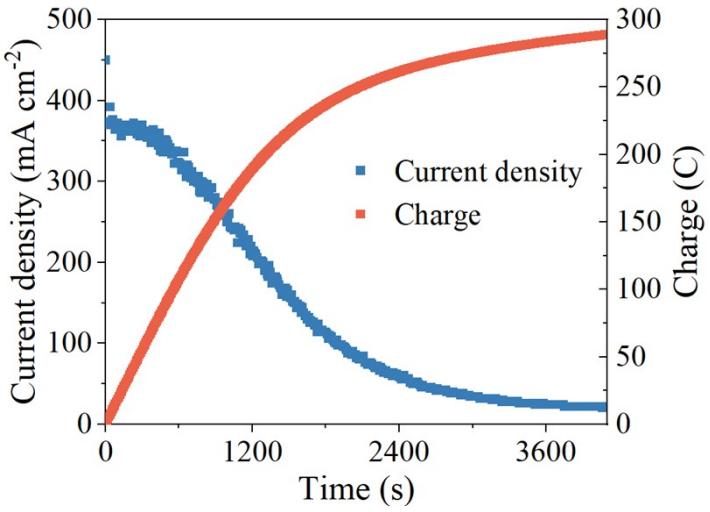

Figure S13. Electrocatalytic i-t curves and charge changes for 50 mM HMF in a 10 mL at a potential of 1.55 V vs.RHE.

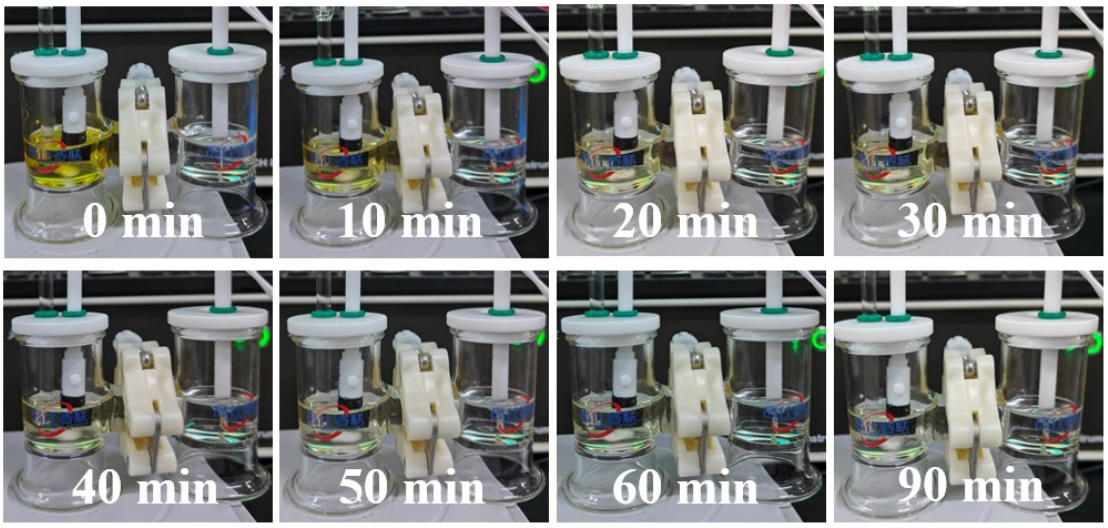

Figure S14. Photographs of the HMF solution during electro-oxidation.

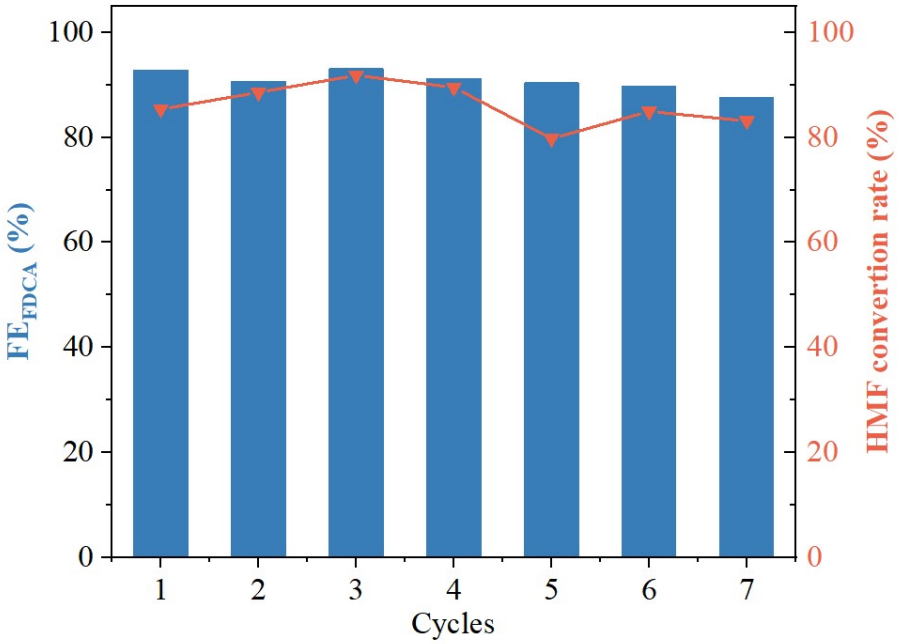

Figure S15. The cyclic stability of the CuNiO electrode

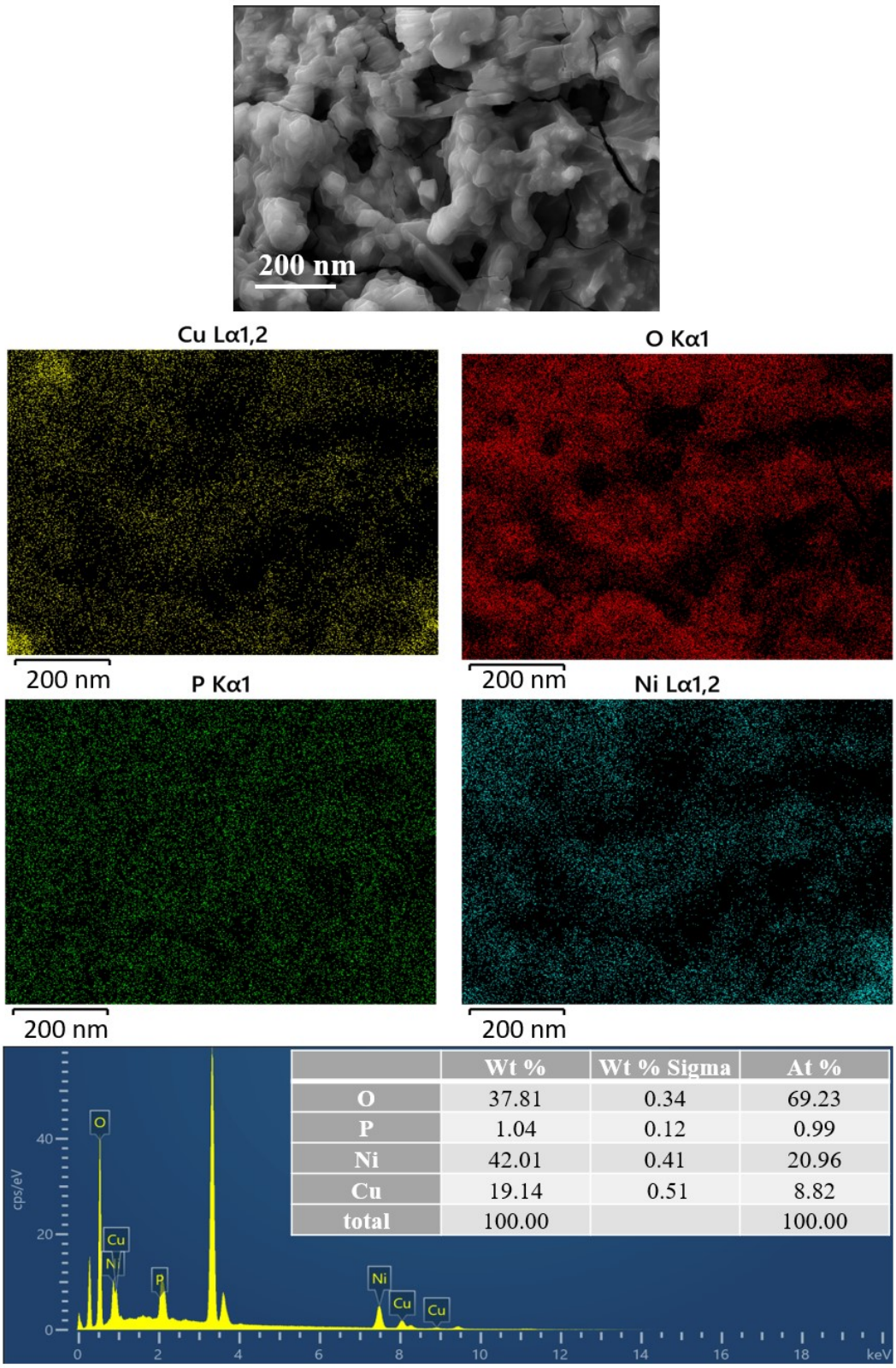

	Wt %	Wt % Sigma	At %
O	37.81	0.34	69.23
P	1.04	0.12	0.99
Ni	42.01	0.41	20.96
Cu	19.14	0.51	8.82
total	100.00		100.00

Figure S16. SEM-EDS results of PO_4-BPL/CuNiO electrode after 36 cycles

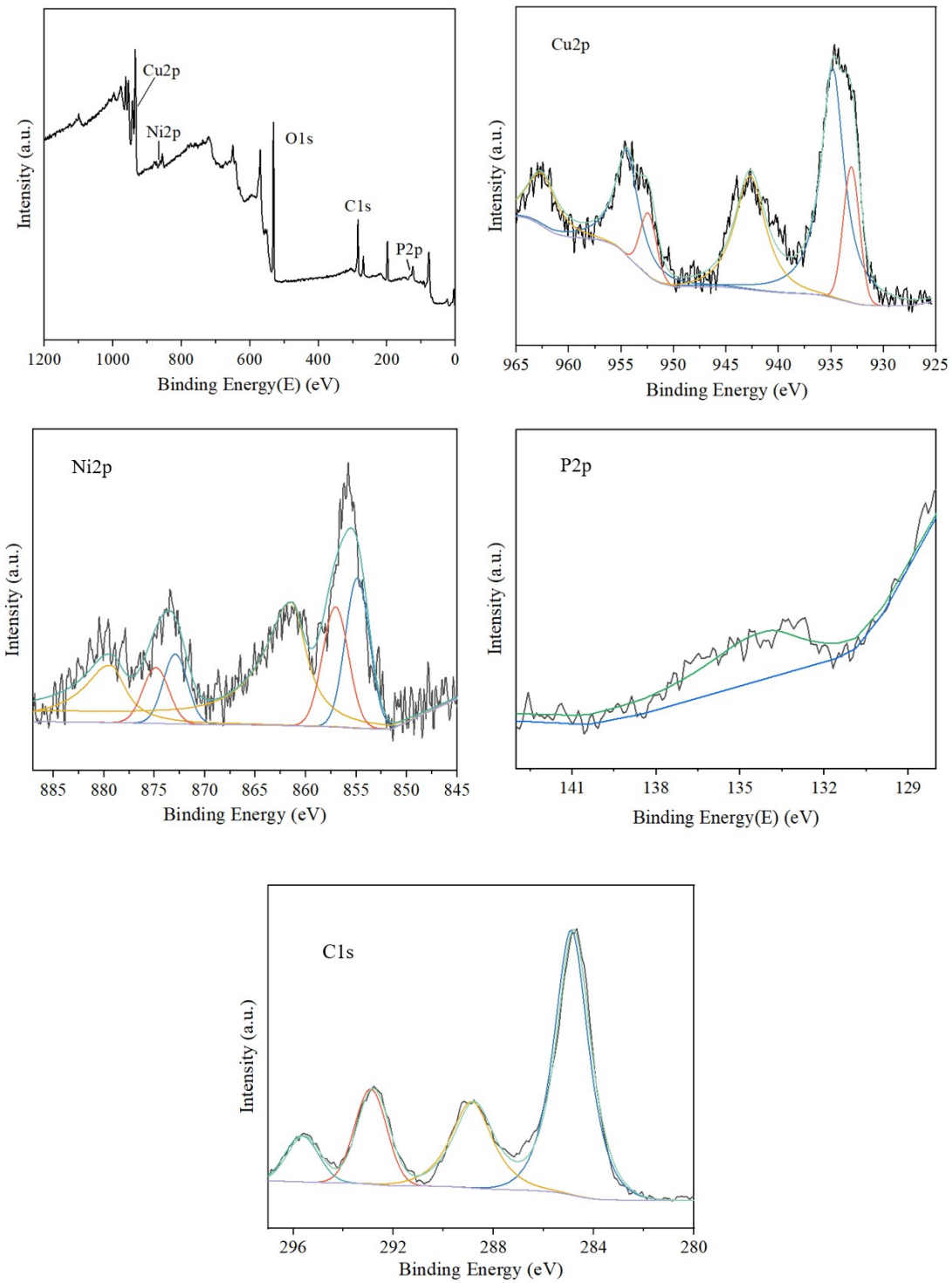

Figure S17. XPS results of PO_4-BPL/CuNiO electrode after 36 cycles

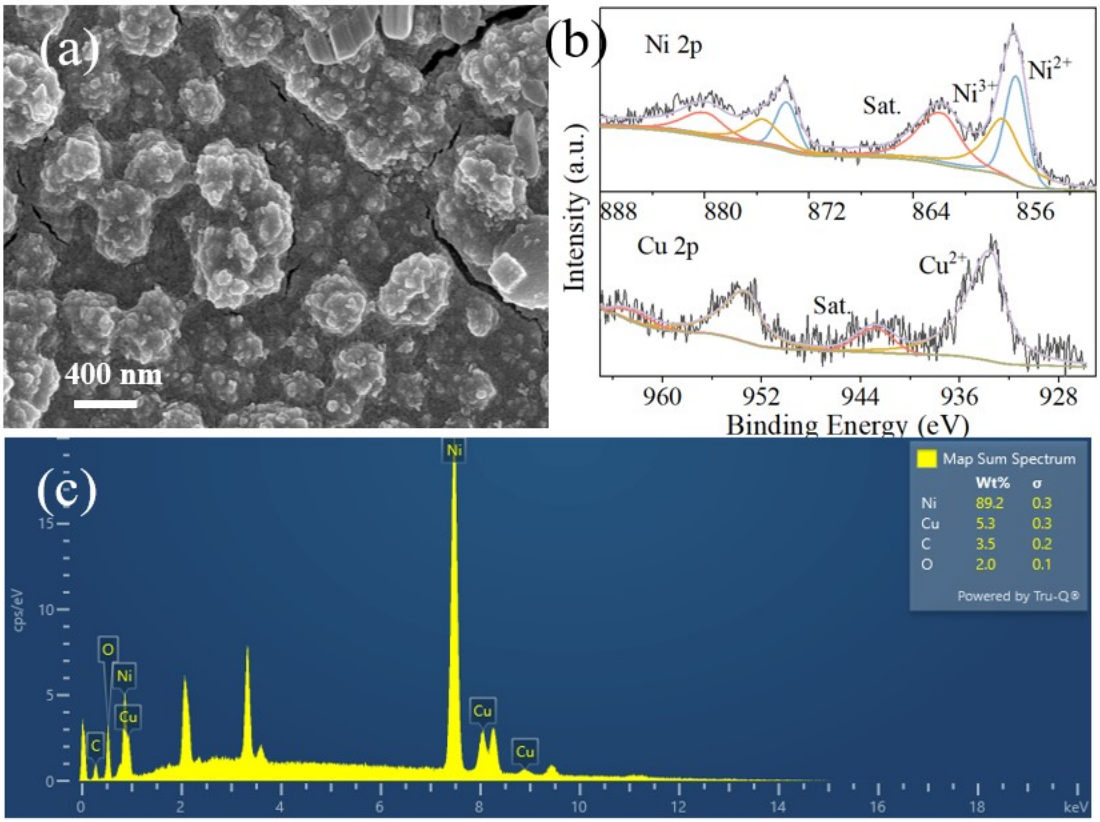

Figure S18. SEM structure and XPS results after CuNiO cycling.

Table S2. Atomic percentage in XPS results after CuNiO cycling

Element	Atomic %
C	52.88
Cu	0.84
Ni	2.68
O	43.06

The EDS mapping results show that the Cu content of the active components on the surface of the catalyst without PO_4-BPL protection has significantly decreased, while the Ni content has significantly increased. The XPS content analysis results indicate that the atomic percentages of both Cu and Ni do not exceed 5%. Therefore, the high Ni content in the EDS mapping results may be due to interference from the substrate foam nickel signal.

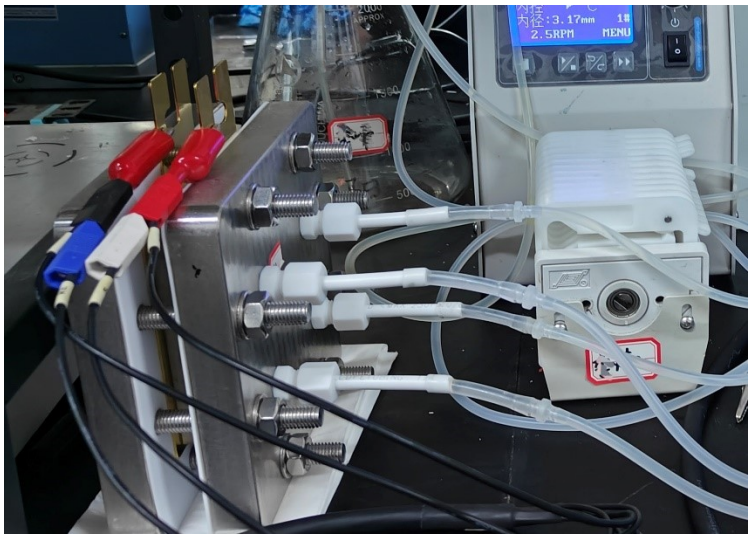

Figure S19. Device diagram of the continuous-flow electrolyzer

Flow electrolyzer details: The area of the electrolytic cell flow channel is 2 cm * 2 cm, the area of the shell is 15 cm*15 cm, the material of the flow channel plate is Ti, the shell is made of stainless steel 316, the gold-plated copper plate is used as the conductive plate of the anode and cathode, and PTFE gasket (1 mm) is used to separate the conductive plate and the shell. An Ivium electrochemical workstation was used to supply voltage to the cell and monitor current changes.

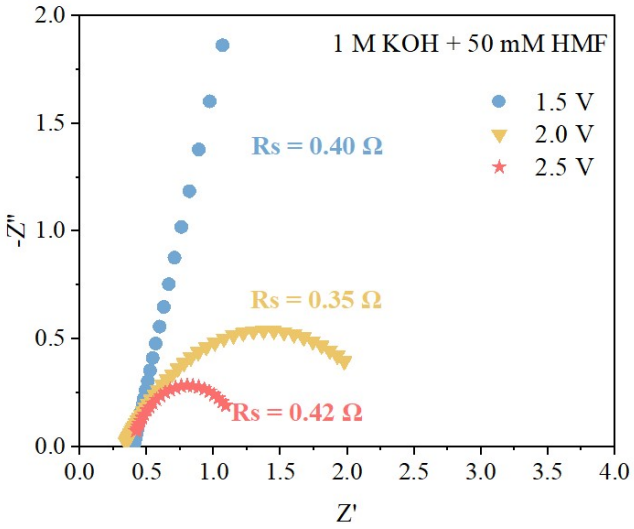

Figure S20. EIS spectra of the flow electrolyzer measured at different applied voltages in 1 M KOH + 50 mM HMF electrolyte.

The mass transfer voltage drop decreases with increasing applied potential in the flow electrolyzer, while the internal resistance (Rs) remains relatively constant. The Ohmic loss value across three potentials was determined to be 0.39 Ω.

Table S3. Comparison of electrocatalytic HMF performance of catalysts recently reported.

Electrocatalysts	Maximum current density[mA/cm^2]	Con [%]	Sel. [%]	FE_{FDCA} [%]	Cyclic performance	Stability time [h]	Ref.
PO_4-BPL/CuNiO	700	99.8	98.7	99.3	36	70	This work
PO_4/Ru-Ni(OH)$_2$	1000	98	99	96	6	4	[1]
$Mn_{0.2}$NiS/GF	500	97.6	98.3	94.2	10	1.67	[2]
$NiCo_2$@MoO_2	220	100	99	99.2	5	6	[3]
Cu/Ni_3S_2	200	100	100	100	6	12	[4]
CoNiS@NF	497	100	100	99.1	11	2.5	[5]
Ni(OH)$_2$/Cu(OH)$_2$	1300	99	97	98-	6	127	[6]
Rh-NiFe	60	-	-	100	6	6.9	[7]
NiCo-LDH	150	-	-	93	5	16.7	[8]
NiO-Co_3O_4	110	95	93	96	-	-	[9]
Ni(OH)$_2$/NF	84	100	-	99	5	1.5	[10]
Ni_3S_2/NiOx	366	-	-	98	-	100	[11]
NiCo-P	150	-	85.8	81.9	8	-	[12]
Ru-Fe single-atom catalysts	-	100	99	98.6	6	-	[13]

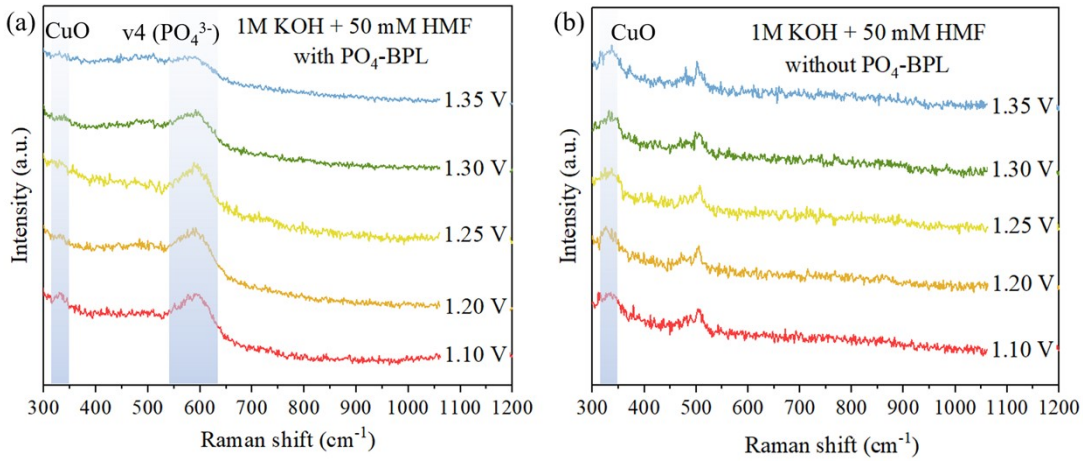

Figure S21. In situ Raman spectroscopy results from 1.1 to 1.35 V vs. RHE in 1 M KOH + 50 mM HMF (a) with PO_4-BPL, (b)without PO_4-BPL.

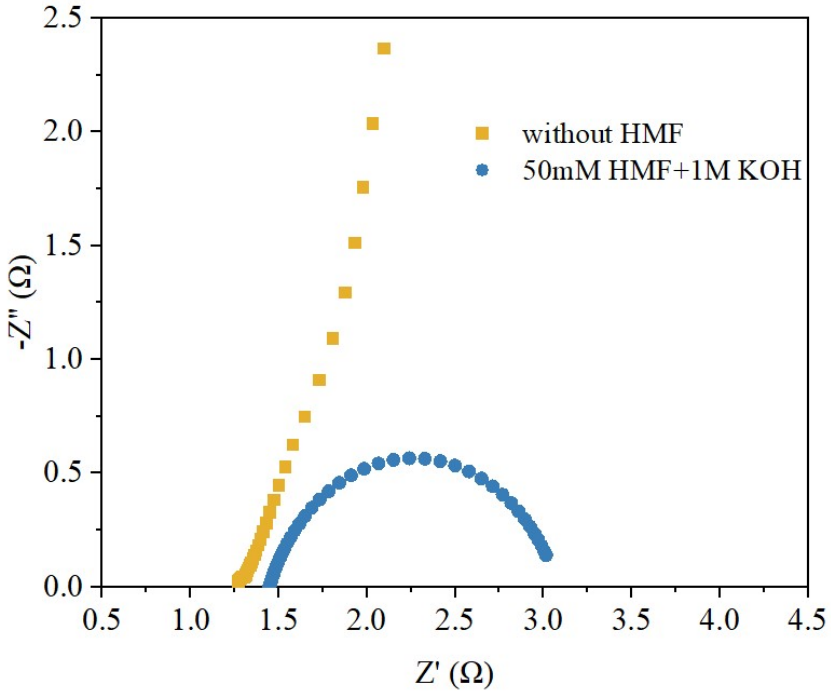

Figure S22. Nyquist plots of PO_4-BPL/CuNiO with and without HMF

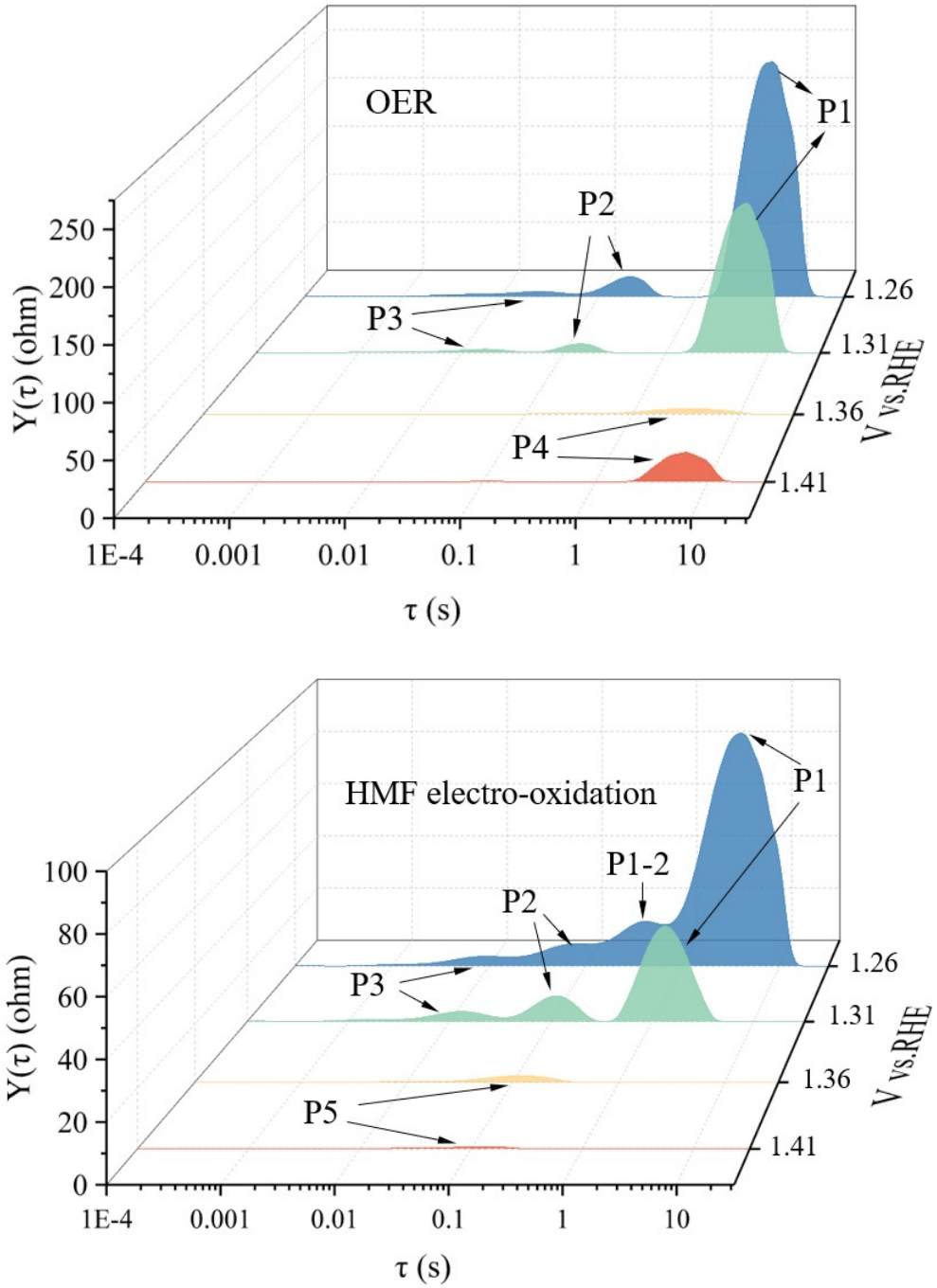

Figure S23. DRT fitting of PO_4-BPL/CuNiO (a) OER and (b) in 50mM HMF solution at different potentials. The P1 peak indicates the ion transfer process of OH^-, P2 corresponds to the proton transfer resistance, P3 represents the fast charge transfer process caused by electrode surface reconstruction. The appearance of the P4 peak signifies the release of reaction products. P1-2 is the HMF adsorption process on the electrode surface. P5 correspond to HMF electro-oxidation process.

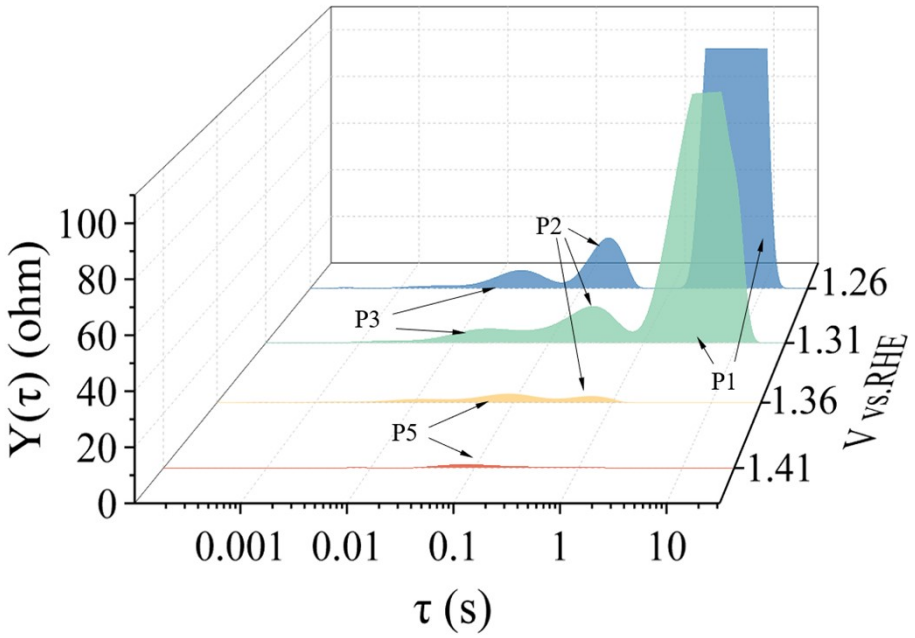

Figure S24. DRT fitting of CuNiO in 50mM HMF solution at different potential.

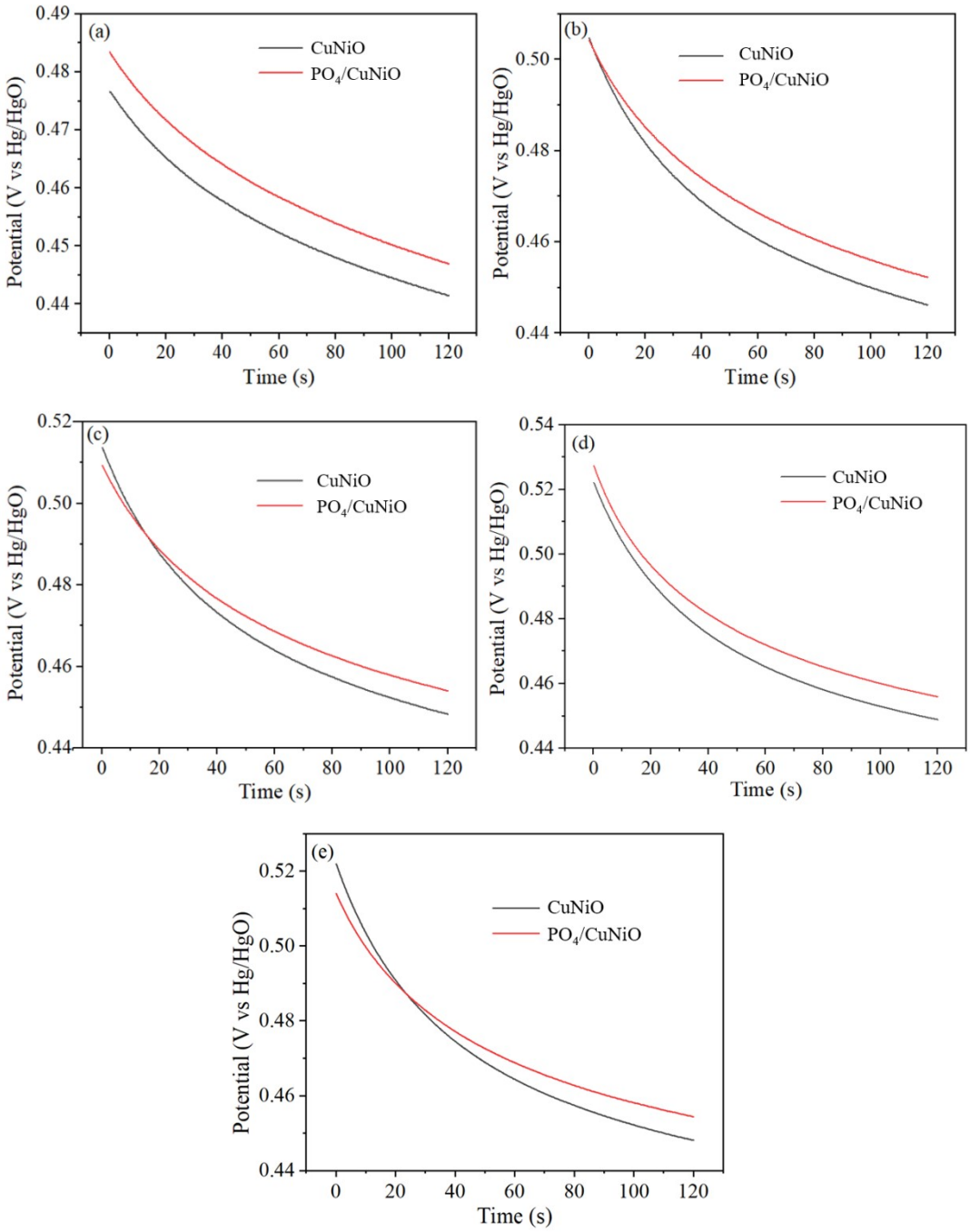

Figure S25. Changes in the open-circuit potential of the PO_4-BPL/CuNiO electrode after application of different potentials (a) 1.45 V, (b) 1.5 V, (c) 1.55 V, (d) 1.6 V, (e) 1.65 V.

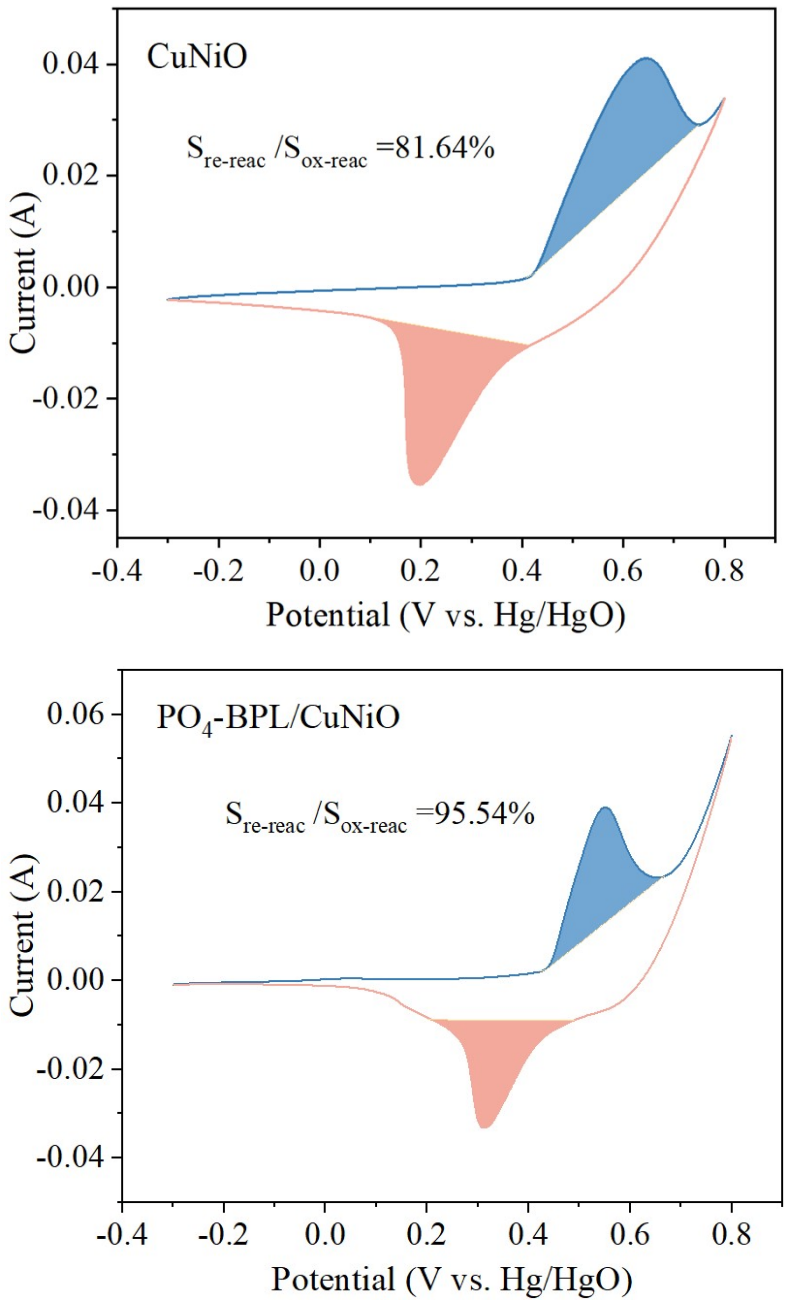

Figure S26. The ratio of the reduction peak area of Ni to the oxidation peak area in the CV curve.

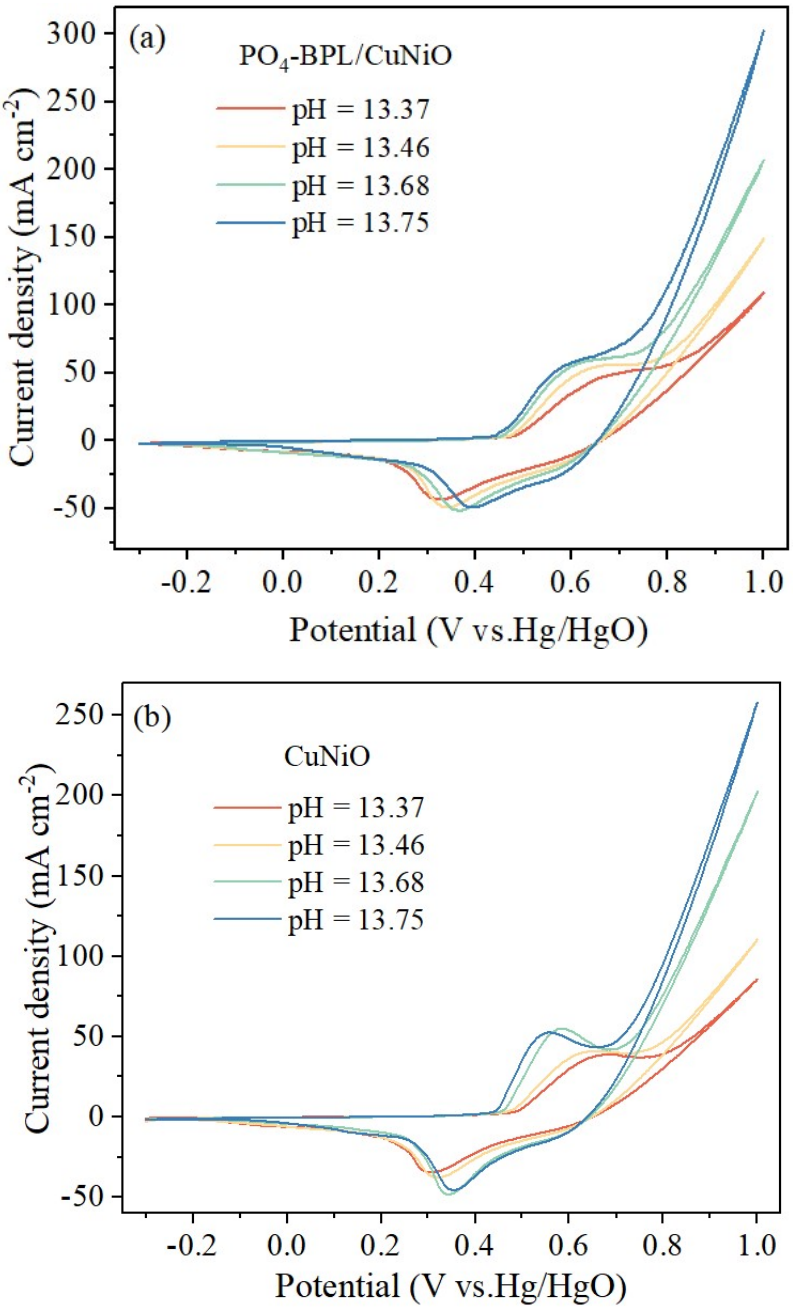

Figure S27. CV curves of (a) PO_4-BPL/CuNiO and (b) CuNiO at different pH

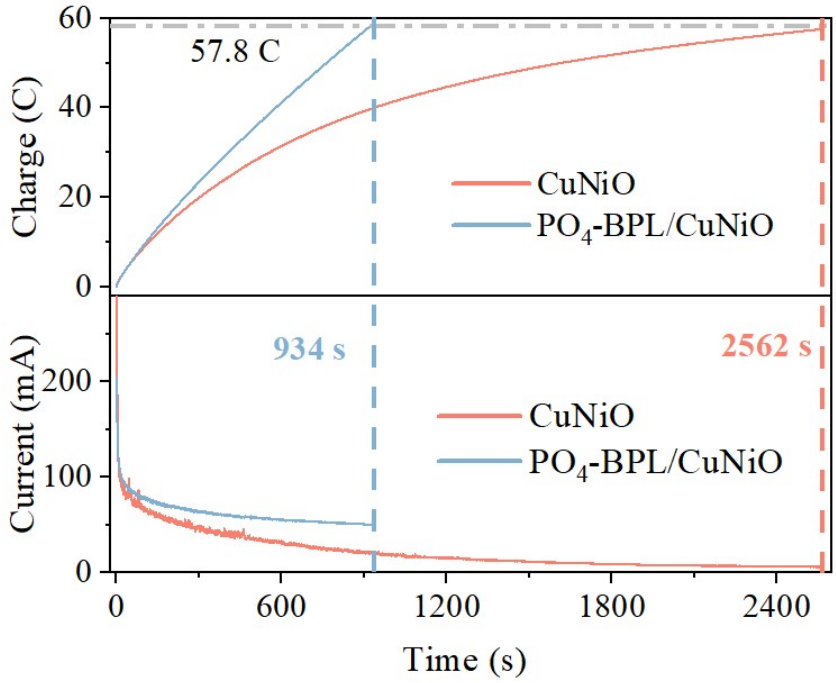

Figure S28. In the presence or absence of PO_4-BPL, the charge current change of 10 ml of 10 mM HMF completely reacting at a potential of 1.55 V vs. RHE.

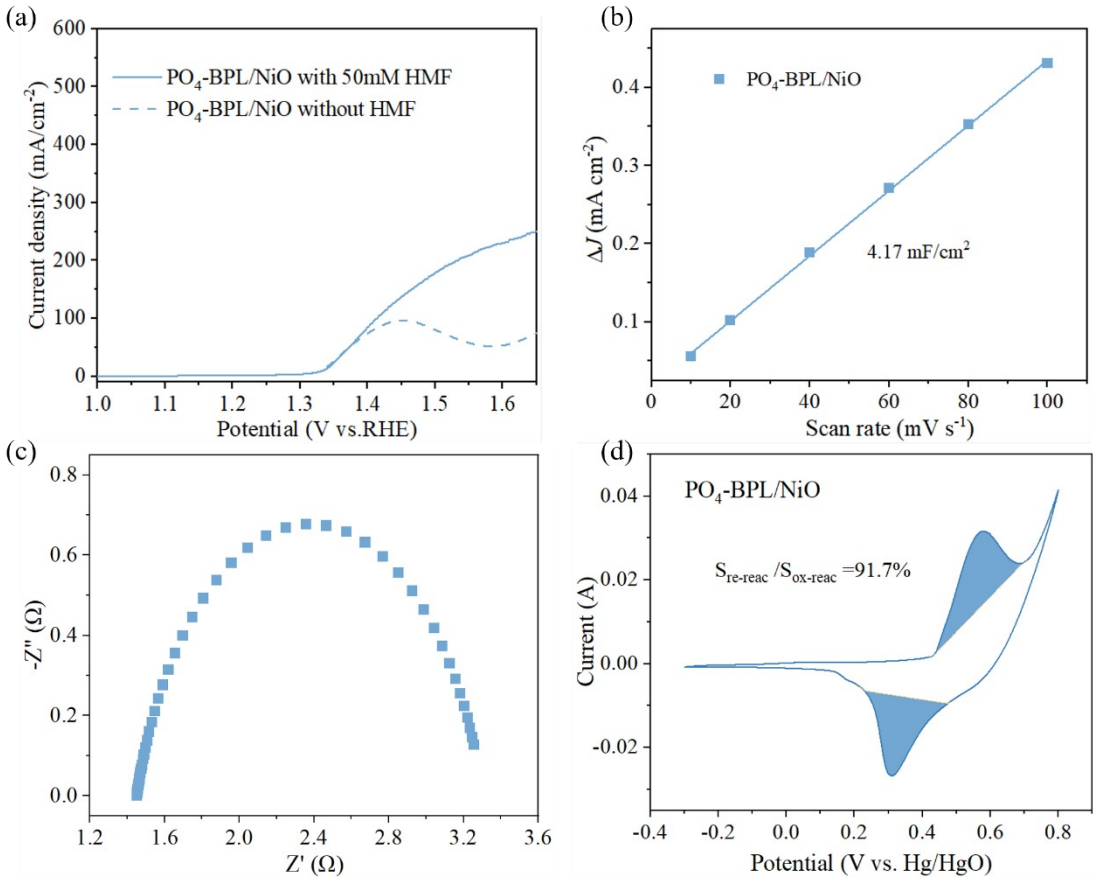

Figure S29. Results of the electrocatalytic performance of PO_4-BPL/NiO (a) LSV curve, (b) the double-layer capacitance, (c) Nyquist plots, (d) the ratio of the reduction peak area of Ni to the oxidation peak area in the CV curve.

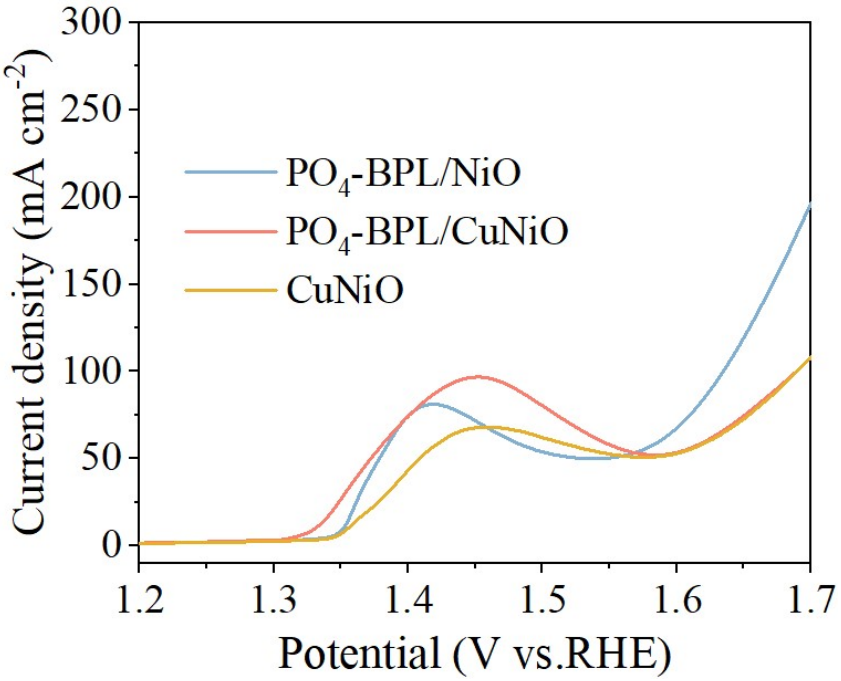

Figure S30. The oxygen evolution under 1M KOH conditions with different catalysts

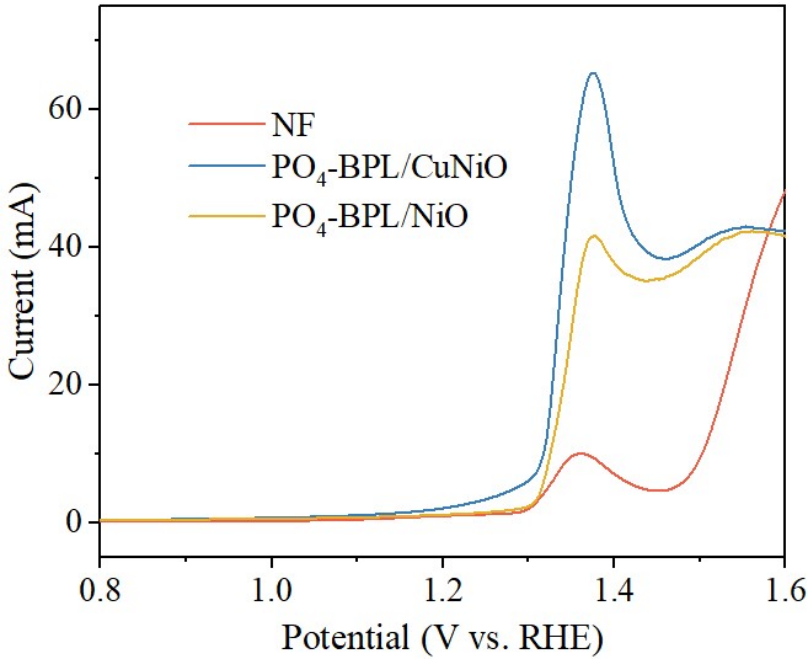

Figure S31. DPV curve of PO_4-BPL/CuNiO, PO_4-BPL/NiO, and NF in 1M KOH

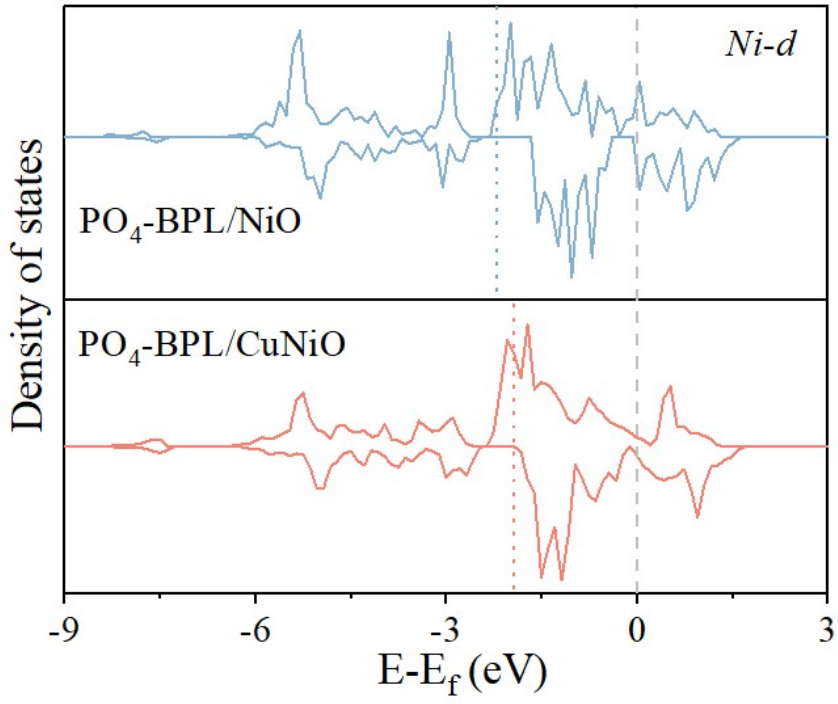

Figure S32. The d-band center and partial densities of states of PO_4-BPL/NiO and PO_4-BPL/CuNiO

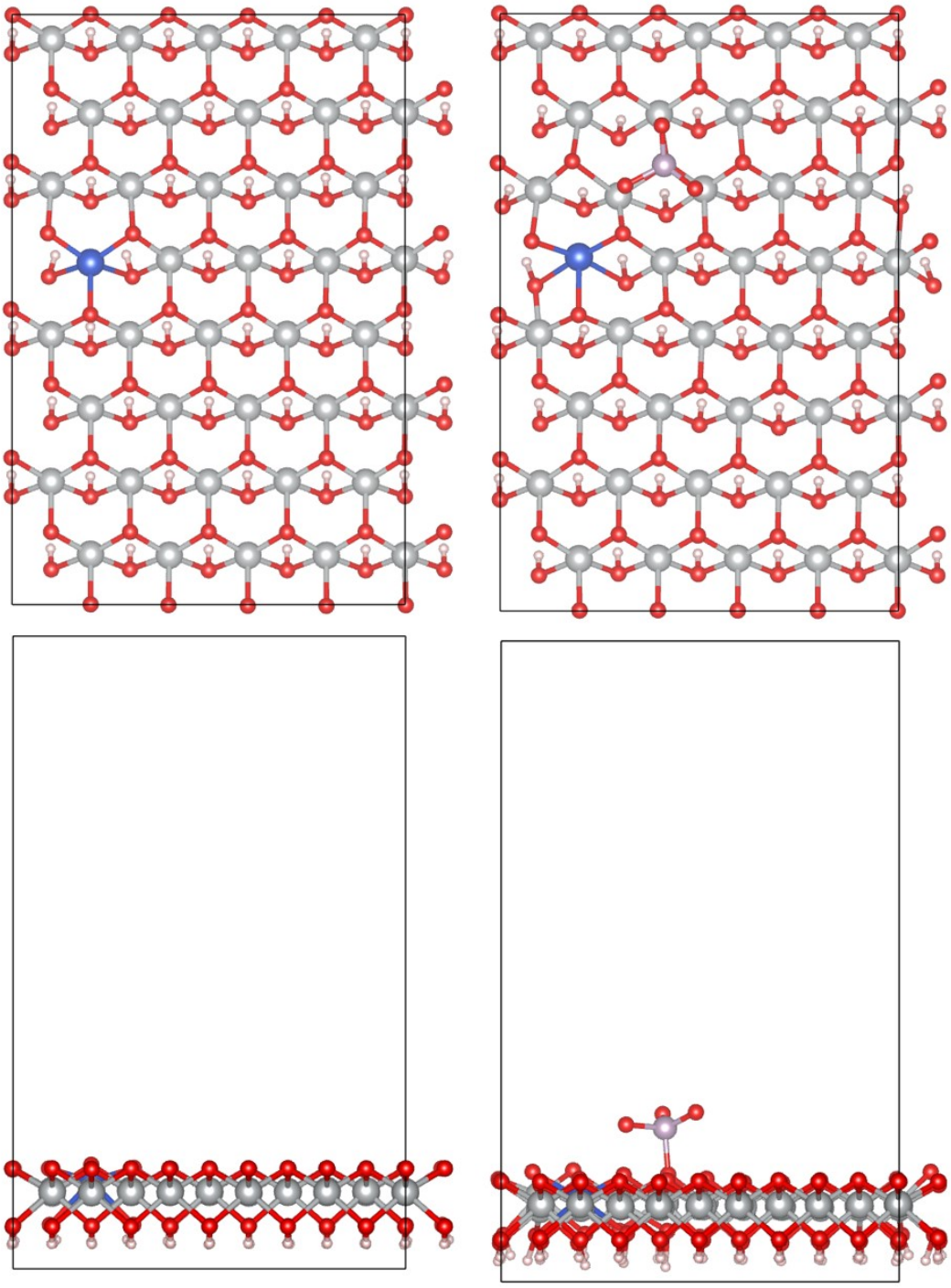

Figure S33. The top and side view of optimized model of CuNiO and PO_4-BPL/CuNiO.

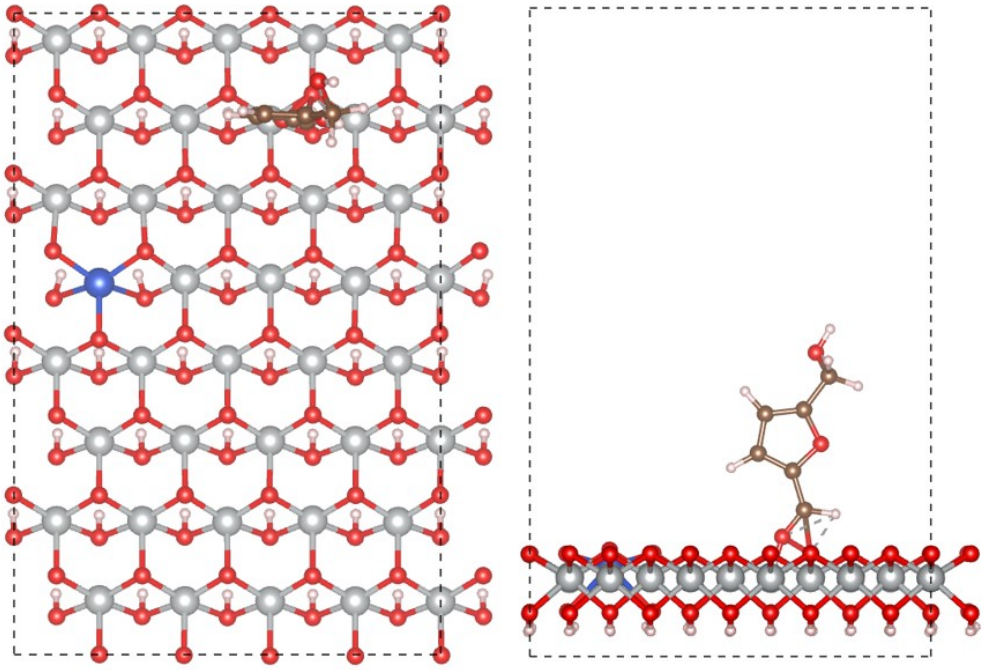

Figure S34. The top and side view of stable configuration of CuNiOOH after HMF adsorption

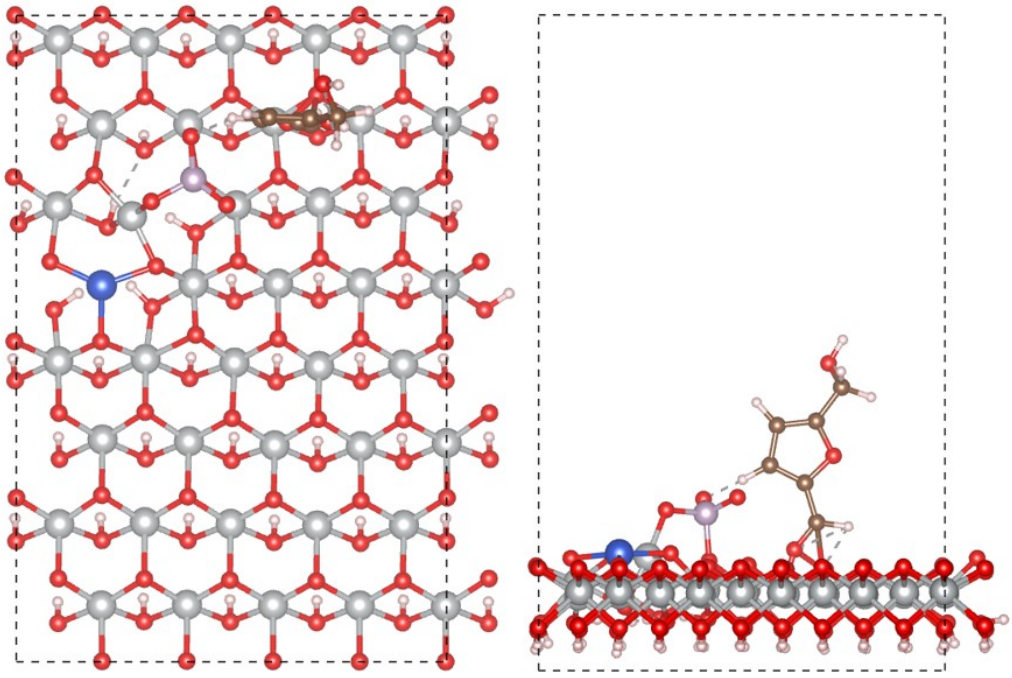

Figure S35. The top and side view of stable configuration of PO4-BPL/CuNiOOH after HMF adsorption

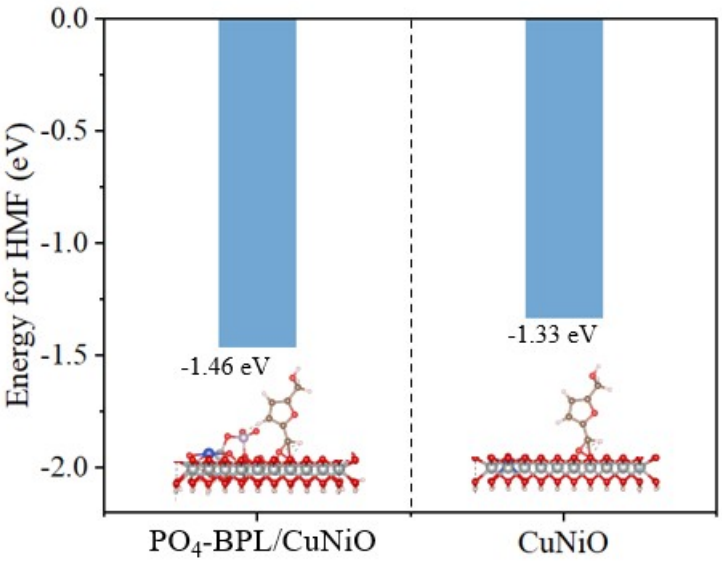

Figure S36. The adsorption free energy of HMF on PO_4-BPL/CuNiO and CuNiO

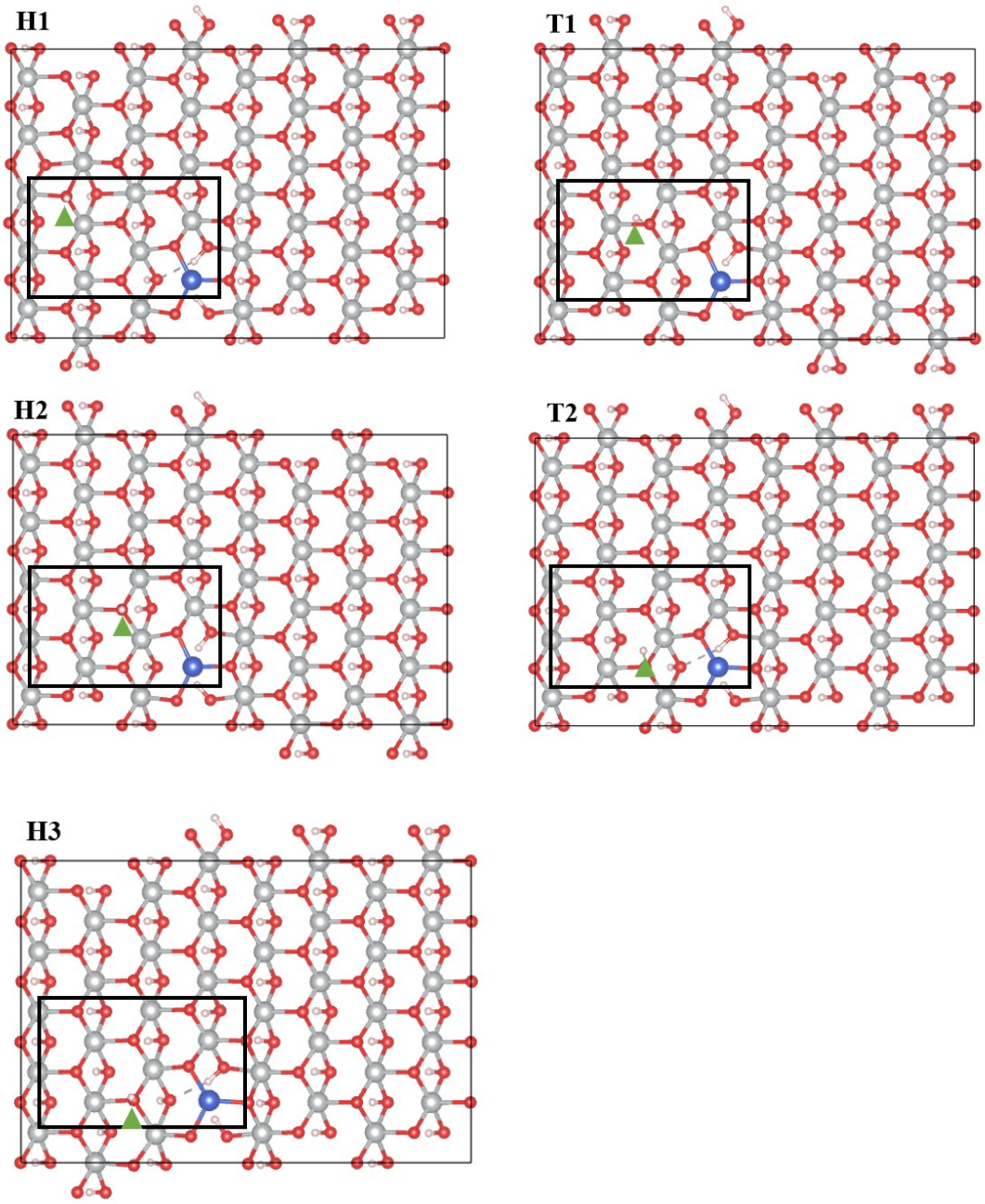

Figure S37. Stable configuration of H protons on the surface of CuNiOOH in the H1-TI-H2-T2-H3 path

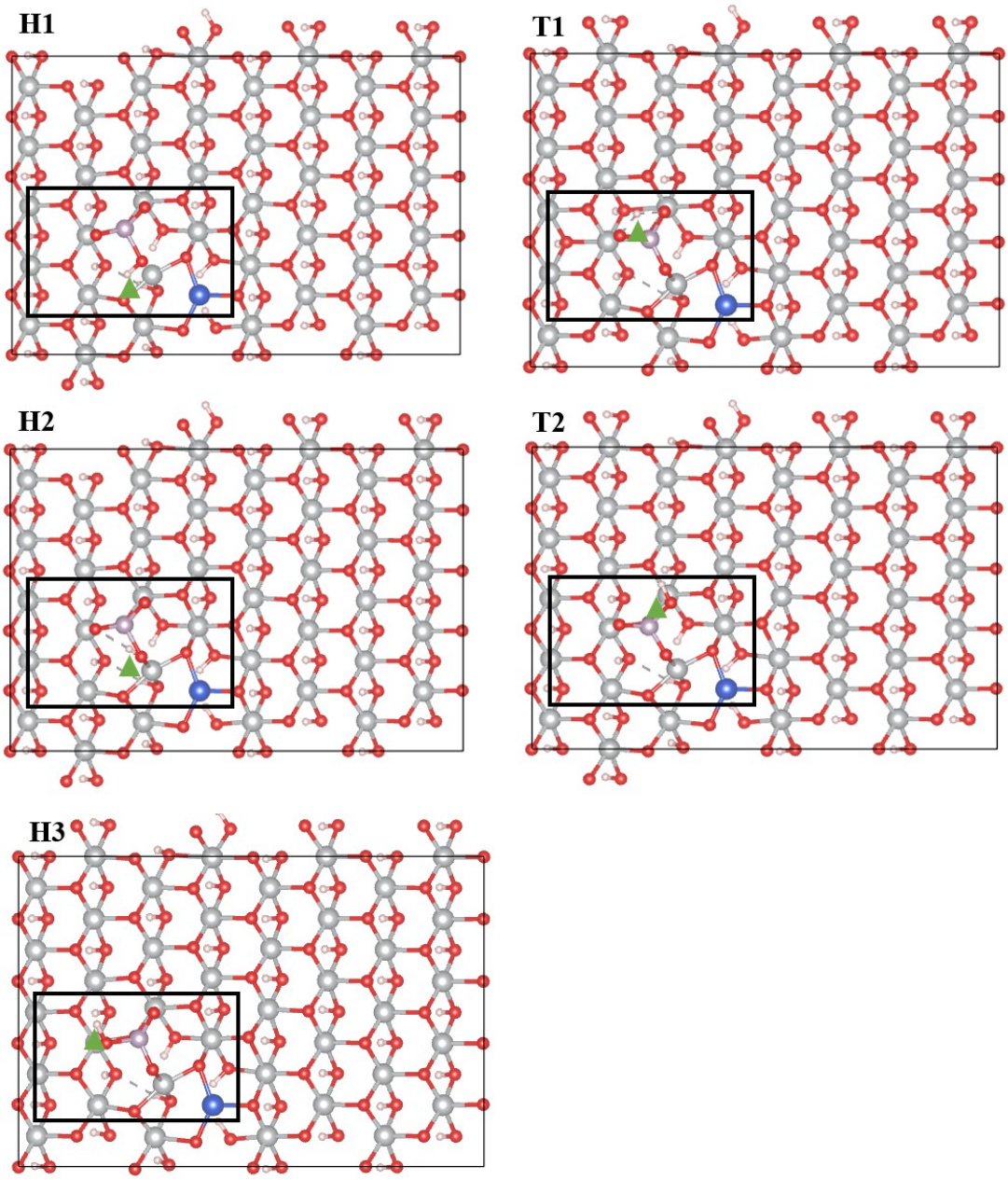

Figure S38. Stable configuration of H protons on the surface of PO_4-BPL/CuNiOOH in the H1-TI-H2-T2-H3 path

References

[1] Z. Yang, S. Wang, C. Wei, L. Chen, Z. Xue, T. Mu, Proton transfer mediator for boosting the current density of biomass electrooxidation to the ampere level, Energy & Environmental Science, 17 (2024) 1603-1611.

[2] S. Li, S. Wang, Y. Wang, J. He, K. Li, Y. Xu, M. Wang, S. Zhao, X. Li, X. Zhong, J. Wang, Doped Mn Enhanced NiS Electrooxidation Performance of HMF into FDCA at Industrial-Level Current Density, Advanced Functional Materials, 33 (2023).

[3] J. Wu, J. Chen, T. Yu, Z. Zhai, Y. Zhu, X. Wu, S. Yin, Boosting Electrochemical Kinetics of NiCo2 via MoO2 Modification for Biomass Upgrading Assisted Hydrogen Evolution, ACS Catalysis, 13 (2023) 13257-13266.

[4] P. Xu, Z. Bao, Y. Zhao, L. Zheng, Z. Lv, X. Shi, H.E. Wang, X. Fang, H. Zheng, Anionic Regulation and Heteroatom Doping of Ni-Based Electrocatalysts to Boost Biomass Valorization Coupled with Hydrogen Production, Advanced Energy Materials, 14 (2023).

[5] Y. Sun, J. Wang, Y. Qi, W. Li, C. Wang, Efficient Electrooxidation of 5-Hydroxymethylfurfural Using Co-Doped Ni3S2 Catalyst: Promising for H2 Production under Industrial-Level Current Density, Advanced Science, 9 (2022).

[6] Z. Yang, L. Chen, Y. Yin, C. Wei, Z. Xue, T. Mu, Weakened hydrogen bond connectivity promotes interfacial mass transfer for industrial level scalable biomass electrooxidation, Energy & Environmental Science, 17 (2024) 8801-8809.

[7] L. Zeng, Y. Chen, M. Sun, Q. Huang, K. Sun, J. Ma, J. Li, H. Tan, M. Li, Y. Pan, Y. Liu, M. Luo, B. Huang, S. Guo, Cooperative Rh-O5/Ni(Fe) Site for Efficient Biomass Upgrading Coupled with H2 Production, Journal of the American Chemical Society, 145 (2023) 17577-17587.

[8] S.-Q. Liu, M.-R. Gao, S. Wu, R. Feng, Y. Wang, L. Cui, Y. Guo, X.-Z. Fu, J.-L. Luo, A coupled electrocatalytic system with reduced energy input for CO2 reduction and biomass valorization, Energy & Environmental Science, 16 (2023) 5305-5314.

[9] Y. Lu, C.-L. Dong, Y.-C. Huang, Y. Zou, Y. Liu, Y. Li, N. Zhang, W. Chen, L. Zhou, H. Lin, S. Wang, Hierarchically nanostructured NiO-Co3O4 with rich interface defects for the electro-oxidation of 5-hydroxymethylfurfural, Science China Chemistry,

63 (2020) 980-986.
[10] J. Zhang, W. Gong, H. Yin, D. Wang, Y. Zhang, H. Zhang, G. Wang, H. Zhao, In Situ Growth of Ultrathin Ni(OH)2 Nanosheets as Catalyst for Electrocatalytic Oxidation Reactions, ChemSusChem, 14 (2021) 2935-2942.
[11] D. Xiao, X. Bao, D. Dai, Y. Gao, S. Si, Z. Wang, Y. Liu, P. Wang, Z. Zheng, H. Cheng, Y. Dai, B. Huang, Boosting the Electrochemical 5-Hydroxymethylfurfural Oxidation by Balancing the Competitive Adsorption of Organic and OH− over Controllable Reconstructed Ni3S2/NiOx, Advanced Materials, 35 (2023).
[12] Y. Song, W. Xie, Y. Song, H. Li, S. Li, S. Jiang, J.Y. Lee, M. Shao, Bifunctional integrated electrode for high-efficient hydrogen production coupled with 5-hydroxymethylfurfural oxidation, Applied Catalysis B: Environmental, 312 (2022).
[13] H. Liu, J. Zhang, X. Li, R. Zhang, W. Jia, J. Zhang, Y. Sun, L. Peng, Strong electronic metal-support interaction between Ru nanoclusters and Fe single atoms enables efficient base-free oxidation of 5-hydroxymethylfurfural to 2,5-furandicarboxylic acid, Applied Catalysis B: Environment and Energy, 365 (2025)